Synthesis and Optical Properties of $Li_3Ba_2La_3(MoO_4)_8:Sm^{3+}$ Powders for pcLEDs

Florian Baur[a], Arturas Katelnikovas[b], Simas Sakirzanovas[c], Ralf Petry[d], and Thomas Jüstel[a]

[a] Department of Chemical Engineering, Münster University of Applied Sciences, Stegerwaldstraße 39, 48565 Steinfurt, Germany

[b] Department of Analytical and Environmental Chemistry, Vilnius University, Naugarduko 24, LT-03225 Vilnius, Lithuania

[c] Department of Applied Chemistry, Vilnius University, Naugarduko 24, LT-03225 Vilnius, Lithuania

[d] Merck KGaA, Frankfurter Straße 250, 64291 Darmstadt, Germany

Reprint requests to Prof. Dr. T. Jüstel. Tel.: +49 2551 962205. Fax: +49 2551 962502.
E-mail: tj@fh-muenster.de

Z. Naturforsch. **2014**, *69b*, 183 – 192 / DOI: 10.5560/ZNB.2014-3279
Received October 6, 2013

A series of Sm^{3+}-activated molybdates $Li_3Ba_2(La_{1-x}Sm_x)_3(MoO_4)_8$ with $0 \leq x \leq 1$ (0 % to 100 % Sm^{3+}) have been prepared by the conventional solid-state synthesis method, and their optical properties were investigated. Reflection, excitation and emission spectra were recorded and put in relation to the various $[Xe]4f^5 \rightarrow [Xe]4f^5$ transitions of Sm^{3+}. The positions of the charge transfer bands of Sm^{3+} and Mo^{6+} were resolved by Gaussian peak fitting. Emission spectra recorded at 100 K revealed the Stark sublevels of the Sm^{3+} energy levels. Time-dependent emission measurements of the $^4G_{5/2} \rightarrow {}^6H_{9/2}$ transition were performed to disentangle the influence of temperature and activator concentration on the decay constants. The results are discussed in the context of the structure of the host material. Sm^{3+} occupies two different crystallographic sites at higher activator concentrations, which results in a bi-exponential decay curve. Temperature-dependent emission spectra were recorded to determine the thermal quenching behavior of the material. Internal and external quantum efficiencies (*IQE* and *EQE*) have been calculated. The *IQE* is independent of temperature, while the emission intensity strongly decreases at temperatures higher than 400 K. It is concluded that the photon escape efficiency in $Li_3Ba_2La_3(MoO_4)_8$ correlates with temperature. An *EQE* of 44 % was achieved for the 2 % Sm^{3+} sample, which is comparatively high for Sm^{3+}. Color points and luminous efficacies were calculated. The color point is independent of the Sm^{3+} concentration, but a blue-shift was observed with increasing temperature. This shift may be caused by lattice expansion and a subsequent decrease of spin-orbit coupling.

Key words: Time- and Temperature-dependent Luminescence, Molybdates, Sm^{3+} Luminescence and Quenching, Phosphors for LEDs

Introduction

Solid-state light (SSL) sources will replace conventional light sources in the next decade [1, 2]. White light-emitting diodes (LEDs) with ever increasing luminous efficacy are being developed [3]. However, phosphor-converted LEDs (pcLEDs) comprising a blue LED and Ce^{3+}-doped garnets as converter emit light with high color temperature and poor color rendering index [4 – 6]. For household application warm-white light, resembling that of incandescent light sources, is generally considered more suitable [7]. This can only be achieved by employing a red-emitting phosphor. Most widely applied are the nitrides $(Ca,Sr,Ba)_2Si_5N_8:Eu^{2+}$ and $(Ca,Sr)AlSiN_3:Eu^{2+}$ [8]. However, these materials require advanced synthesis methods, and the Eu^{2+} emission is rather broad, extending to the deep-red spectral region. This results in a lower luminous efficacy than theoretically possible [9]. Zukauskas *et al.* simulated the emission spectra

of several pcLEDs. They found that for a color temperature of 3500 K and a high color rendering index, the ideal red-emitting phosphor would comprise a low FWHM of < 30 nm with the peak intensity around 655 nm [6]. Eu^{3+} and Mn^{4+} fulfill these requirements and are gaining increased attention [9 – 13]. Sm^{3+}-activated phosphors pose an interesting alternative to these two activator ions as they exhibit a strong emission at around 650 nm and an absorption in the near-UV and blue spectral range [14, 15].

Experimental

Samples of $Li_3Ba_2(La_{1-x}Sm_x)_3(MoO_4)_8$ were prepared by conventional solid state reactions. Stoichiometric amounts of high purity Li_2CO_3 (99.0 %, AlfaAesar), $BaCO_3$ (99.0 %, AlfaAeasar), La_2O_3 (99.99 %, Treibacher), MoO_3 (99.5 %, AlfaAesar) and Sm_2O_3 (99.995 %, Treibacher) were thoroughly mixed in an agate mortar employing acetone as grinding medium. The resulting mixtures were dried, transferred to porcelain crucibles and annealed at 800 °C for 10 h in air. A series of phosphors with different Sm^{3+} concentrations ($0 \leq x \leq 1$) was obtained.

XRD data were collected from $5 \leq 2\theta \leq 60°$ using Ni-filtered Cu K_α radiation on a Rigaku MiniFlex II diffractometer working in Bragg-Brentano ($\theta/2\theta$) geometry. Step width and integration time were 0.02° and 1 s, respectively.

SEM images were taken by a FE-SEM Hitachi SU-70. Before the measurements the samples were coated by a thin chromium film to avoid charging.

Reflection spectra were recorded on an Edinburgh Instruments FS900 spectrometer equipped with a 450 W Xe arc lamp, a cooled (−20 °C) single-photon counting photomultiplier (Hamamatsu R928) and an integration sphere coated with barium sulfate. $BaSO_4$ (99 %, Sigma-Aldrich) was used as a reflectance standard. The excitation and emission slits were set to 10 and 0.06 nm, respectively.

Excitation and emission spectra were recorded on an Edinburgh Instruments FSL900 spectrometer equipped with a 450 W Xe arc lamp, mirror optics for powder samples and a cooled (−20 °C) single-photon counting photomultiplier (Hamamatsu R2658P). The photoluminescence emission spectra were corrected by a correction file obtained from a tungsten incandescent lamp certified by the NPL (National Physics Laboratory, U. K.). When measuring emission spectra excitation and emission slits were set to 5 and 0.5 nm, respectively.

For thermal quenching (TQ) measurements a cryostat MicrostatN from Oxford Instruments was attached to the spectrometer. Liquid nitrogen was used as a cooling agent. Temperature stabilization time was 60 s and tolerance set to ±5 K. Measurements were carried out from 100 to 500 K in 50 K steps.

The PL decay kinetics studies were performed on an Edinburgh Instruments FSL900 spectrometer equipped with a Xe μs-flash lamp.

Quantum efficiencies (*QE*) were calculated by measuring the emission spectrum of a $BaSO_4$ sample in a barium sulfate-coated integration sphere. The excitation monochromator was set to 404.5 nm, and reflection and emission from the sample in the range of 375 to 800 nm were recorded. The same measurement was repeated for the phosphor sample. The *QE* can be calculated using the formula:

$$QE = \frac{\int I_{\mathrm{em,phosphor}} - \int I_{\mathrm{em,BaSO_4}}}{\int I_{\mathrm{abs,BaSO_4}} - \int I_{\mathrm{abs,phosphor}}} \times 100\,\% \qquad (1)$$

where $\int I_{\mathrm{em,\ phosphor}}$ and $\int I_{\mathrm{em,\ BaSO_4}}$ are integrated emission intensities of the phosphor and $BaSO_4$, respectively. Similarly, $\int I_{\mathrm{abs,\ phosphor}}$ and $\int I_{\mathrm{abs,\ BaSO_4}}$ are the integrated absorptions of the phosphor and of $BaSO_4$, respectively. In other words, the amount of emitted photons is divided by the amount of absorbed photons.

Results and Discussion

XRD patterns as depicted in Fig. 1 strongly indicate the presence of a complete solid solution series from 0 to 100 % Sm^{3+}. The XRD pattern of $Li_3Ba_2Gd_3(MoO_4)_8$ [16] was used as a reference as to the best of our knowledge no reference for either the La^{3+} or Sm^{3+} compound has been published yet.

In the reflection spectrum of $Li_3Ba_2Sm_3(MoO_4)_8$ (Fig. 2, gray line) the $4f$-$4f$ transitions of Sm^{3+} are easily distinguished, and their positions are in good agreement with the values reported elsewhere [17 – 19]. All visible transitions originate from the $^6H_{5/2}$ ground level and are *intra*-configurational ($[Xe]4f^5 \rightarrow [Xe]4f^5$) with $\Delta l = 0$. This renders them forbidden according to the Laporte rule. The majority of these transitions can be assigned to induced electric dipole interactions with the selection rule $\Delta J \leq 6$. However, there are magnetic dipole transitions with $J = 0$, such as the $^6H_{5/2} \rightarrow {}^4G_{5/2}$ transition at 563 nm [19]. Additionally, most of the transitions are spin-forbidden due to a change in spin multiplicity, namely from $S = 6$ to $S = 4$. Therefore, the absorption strength is rather weak. The most intense $[Xe]4f^5 \rightarrow [Xe]4f^5$ absorption lines can be observed at 404.5 nm and originate from three separate transitions, *i. e.* from the $^6H_{5/2}$ ground level to $^4L_{13/2}$, $^6P_{3/2}$ and $^4F_{7/2}$. The undoped sample (black line) shows

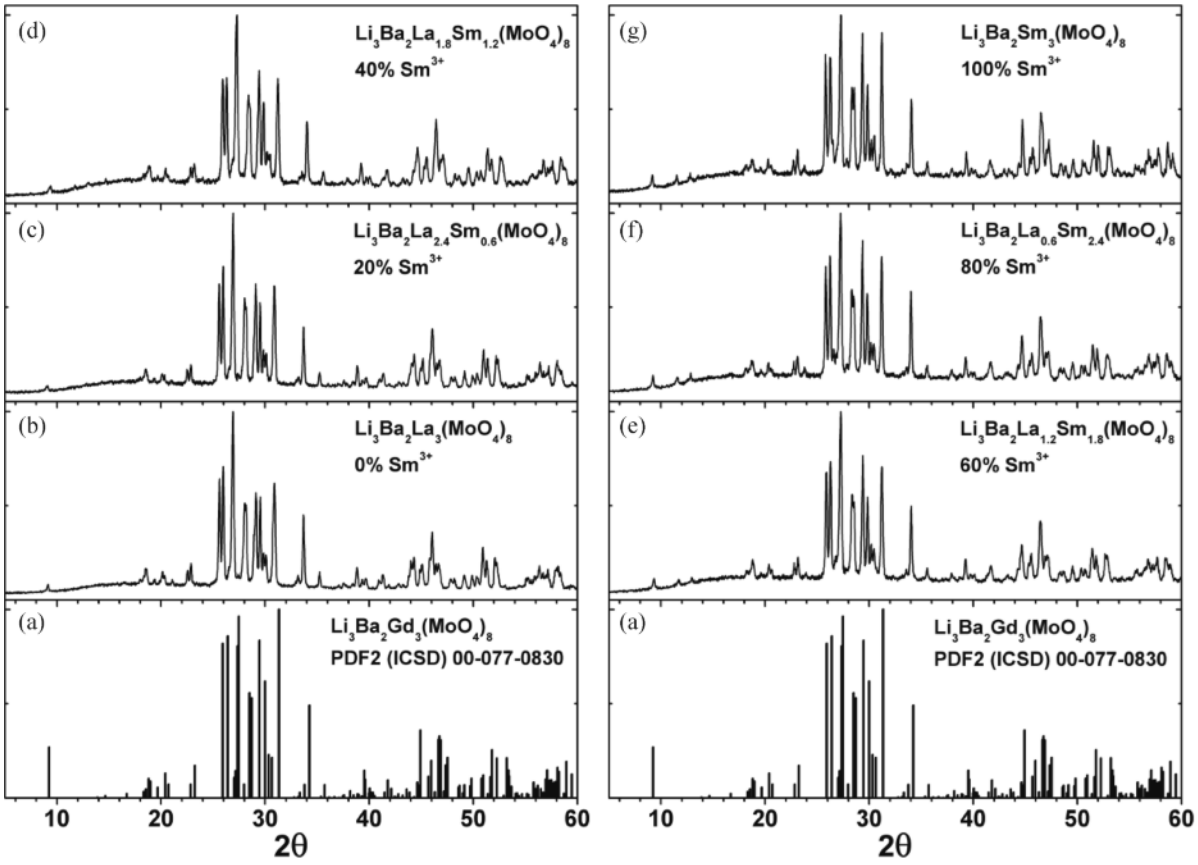

Fig. 1. XRD patterns of $Li_3Ba_2(La_{1-x}Sm_x)_3(MoO_4)_8$ samples with different Sm^{3+} concentrations: (a) reference pattern of $Li_3Ba_2Gd_3(MoO_4)_8$ [PDF2 (ICSD) 00-077-0830]; (b) 0 % Sm^{3+}; (c) 20 % Sm^{3+}; (d) 40 % Sm^{3+}; (e) 60 % Sm^{3+}; (f) 80 % Sm^{3+}; (g) 100 % Sm^{3+}.

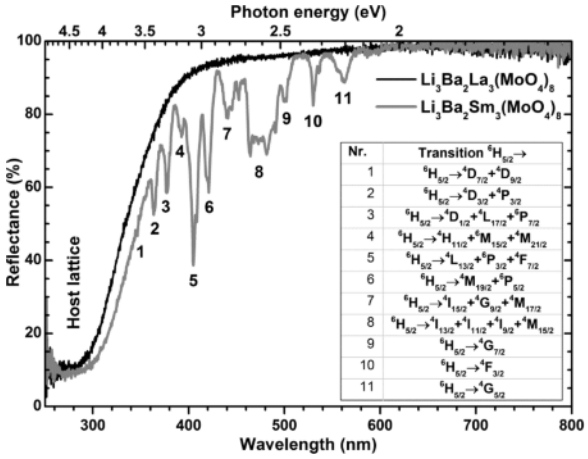

Fig. 2. Reflection spectra of (black line) $Li_3Ba_2La_3(MoO_4)_8$ and (gray line) $Li_3Ba_2Sm_3(MoO_4)_8$. Transitions and their respective numbers are listed in the table.

nearly 100 % reflectivity in the range from 400 to 800 nm with a strong absorption around 300 nm which can be assigned to $O^{2-} \rightarrow Mo^{6+}$ charge transfer (CT) of the host structure. From the turning point of the absorption edge the optical band gap of the undoped material was calculated to be about 3.65 eV. This value is identical to that published by Katelnikovas *et al.* [9]. In the 100 % Sm^{3+} sample this absorption can be observed as well, however, slightly broadened. The same broadening was reported to occur in Eu^{3+}-activated $Li_3Ba_2La_3(MoO_4)_8$ [9]. It is assigned to overlapping host structure absorption and $[MoO_4]^{2-} \rightarrow Sm^{3+}$ CT bands.

In the excitation spectrum recorded by monitoring the emission at 645 nm as depicted in Fig. 3a all aforementioned transitions can be observed as well. It is possible to pump the Sm^{3+} ion *via* a broad excita-

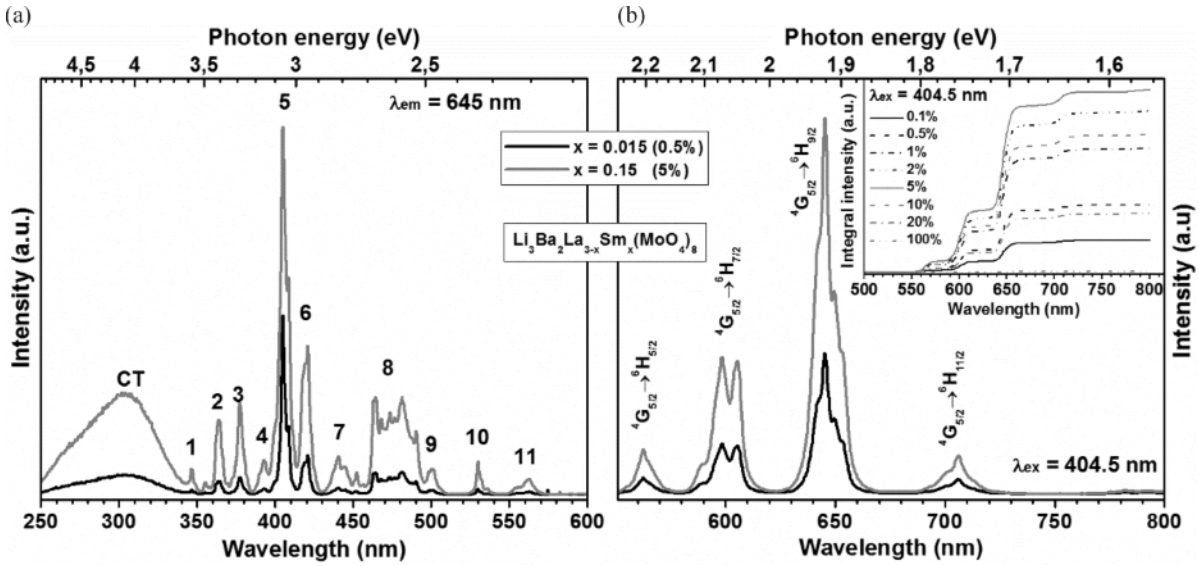

Fig. 3. Luminescence spectra of $Li_3Ba_2(La_{1-x}Sm_x)_3(MoO_4)_8$ with (black) $x = 0.015$ (0.5 %) and (gray) $x = 0.15$ (5 %); (a) excitation spectra of 615 nm emission with transitions marked with numbers, see inset table in Fig. 2; (b) emission spectra upon 404.5 nm excitation and (inset) normalized emission integrals thereof.

tion band in the UV-C/B spectral range. The asymmetric nature of the band substantiates the claim that the absorption in this spectral region consists of both an $O^{2-} \rightarrow Mo^{6+}$ and a $[MoO_4]^{2-} \rightarrow Sm^{3+}$ CT band. A Gaussian peak fitting ($R^2 = 0.998$) yielded two bands, peaking at 32 260 cm^{-1} (310 nm, 4.01 eV) and 35 460 cm^{-1} (282 nm, 4.40 eV), respectively. Taking the redox potential of the metal centers into account, the higher energy band is tentatively assigned to the Sm^{3+} CT and the lower energy band to the Mo^{6+} CT. Additionally, the value of 4.40 eV agrees well with that of 4.33 eV for Sm_2O_3 thin films published by Dakhel [20]. Two more line multiplets are of interest. The lines located around 404 nm (line 5 in Fig. 2) can be employed to excite the material *via* a near UV emitting LED. Additionally, absorption at this spectral position is relatively strong, approaching 65 %. Furthermore, excitation with a 465 nm blue LED is possible due to a broad line multiplet (line 8 in Fig. 2) located between 460 and 490 nm. These properties brand Sm^{3+}-activated phosphors as potential candidates for application in pc LEDs. The relative intensities of different transitions do not change with the activator concentration (black line: 0.5 % Sm^{3+}, gray line: 5 % Sm^{3+}).

In Fig. 3b the emission spectra of $Li_3Ba_2(La_{1-x}Sm_x)_3(MoO_4)_8$ (black line: 0.5 % Sm^{3+}, gray line: 5 % Sm^{3+}) are depicted. Emission in the visible range is caused by transitions from the $^4G_{5/2}$ level to the different ^5H_J manifolds, followed by relaxation to the ground state. Radiative transitions to the ^6F_J manifolds occur as well, but result in emission in the NIR range [21]. The $^4G_{5/2}$ level can be populated by relaxation from higher energy levels or directly from the $^6H_{5/2}$ ground state by excitation with 563 nm radiation. For the measurement the sample was excited with 404.5 nm radiation. The dominant emission line is peaking at 645 nm, corresponding to the $^4G_{5/2} \rightarrow ^6H_{9/2}$ transition. Each line multiplet consists of several components. Due to electron-phonon interaction, causing line broadening, the peaks are not well resolved at room temperature. They can be more readily distinguished when recording the emission at 100 K (Fig. 4a). The splitting of a single transition line into several components is the result of the crystal field generated by the O^{2-} ligands acting on the Sm^{3+} central atom. In case of half-integer spin ions like Sm^{3+}, each $^{2S+1}L_J$ multiplet is split up into $J + 1/2$ Stark sublevels [17, 22].

The inset in Fig. 3 depicts the normalized integrated emission intensity of $Li_3Ba_2(La_{1-x}Sm_x)_3(MoO_4)_8$ for different values of x. The emission integral increases with increasing Sm^{3+} concentration until it reaches a maximum at an activator concentration of 5 %. A fur-

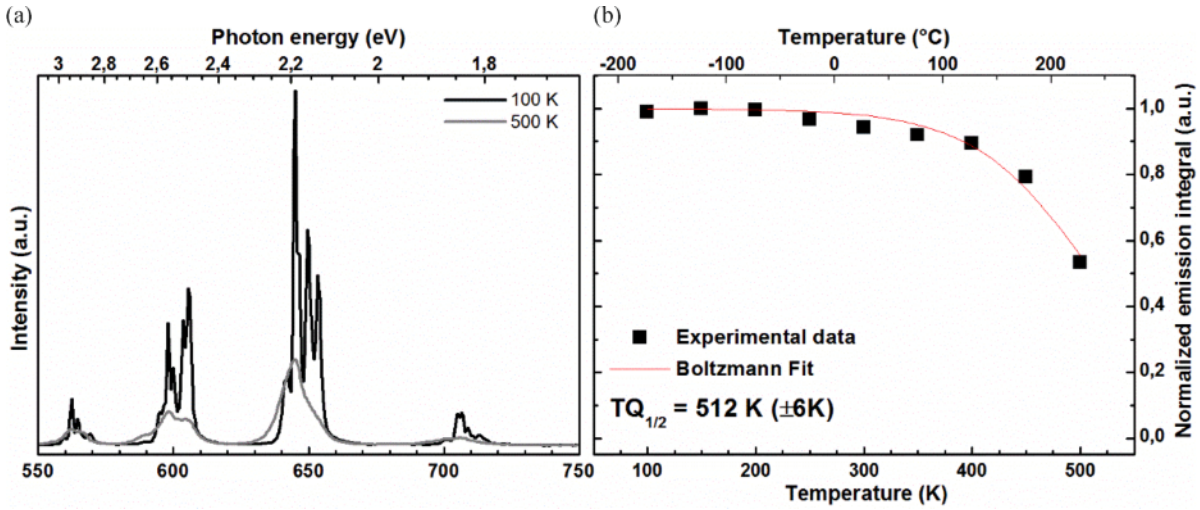

Fig. 4. (a) Normalized emission spectra of $Li_3Ba_2La_3(MoO_4)_8$: Sm^{3+} (5 %) at (black) 100 K and (gray) 500 K upon 404.5 nm excitation; (b) normalized emission integral at different temperatures with Boltzmann fit.

ther increase of the concentration results in a decrease of the emission intensity. Such behavior is indicative of concentration quenching. Quenching processes can be based on exchange interaction or Coulomb interaction (multipolar interaction). It is generally assumed that for exchange interaction to play a role, the mutual separation between two activator ions has to be lower than 0.5 nm [23, 24]. The distance between the activator ions at a given concentration can be calculated using Blasse's equation [25],

$$R_c^3 \approx \frac{24V}{4\pi \cdot x \cdot N} \tag{2}$$

where V is the volume of the unit cell (1.28 nm^3) [16], N is the number of La^{3+} ions per unit cell (6) and x is the concentration of Sm^{3+} at which quenching sets in. Up to a concentration of 1.5 % the emission intensity increases approximately linearly with the activator concentration. Somewhere between the 1.5 and 2 % samples the slope begins to decrease, *i. e.* after this point, every additional Sm^{3+} ion yields less emission intensity than the previous one. Therefore, it can be assumed that concentration quenching sets in as soon as a concentration between 1.5 and 2 % Sm^{3+} has been reached. However, the decay measurements indicate an even earlier onset of concentration quenching (see Fig. 5). For these values the equation results in 3.00 nm $< R_c \lesssim$ 2.73 nm which is well above the 0.5 nm limit. Therefore, a multipolar mechanism is assumed for the concentration quenching in this material. A quenching mechanism based on dipole-dipole interaction has been reported for Sm^{3+} in several oxidic hosts [22, 26, 27]. Most likely cross-relaxation between two Sm^{3+} ions is responsible for the quenching [15, 19, 28]. A transition from the excited $^4G_{5/2}$ state to $^6F_{5/2}$ in one ion resonates with a transition from the $^6H_{5/2}$ ground state to $^6F_{11/2}$ (ΔE = 10 495 and 10 504 cm^{-1}, respectively) in another ion leading to the non-radiative decay to the ground state of both ions [29].

Moreover, the temperature-dependent emission spectra in the range from 100 to 500 K for the 5 % Sm^{3+}-doped sample were recorded. The results are presented in Fig. 4. On the left hand side (a) the 100 and 500 K emission spectra are depicted. As mentioned previously, in the emission spectrum recorded at 100 K the lines are partly resolved to their respective Stark components. With increasing temperature the individual components broaden, and the intensity decreases. At 500 K the peaks have broadened so much that the components are not distinguishable any more. The decrease in emission intensity is caused by thermal quenching. Thermal quenching can occur by tunneling due to a large Stokes Shift, however, transitions within the 4f shell exhibit a very small Stokes Shift. Therefore, photoionization is a likely cause of the observed quenching process. By calculating the integrated emission intensity and plotting it against tem-

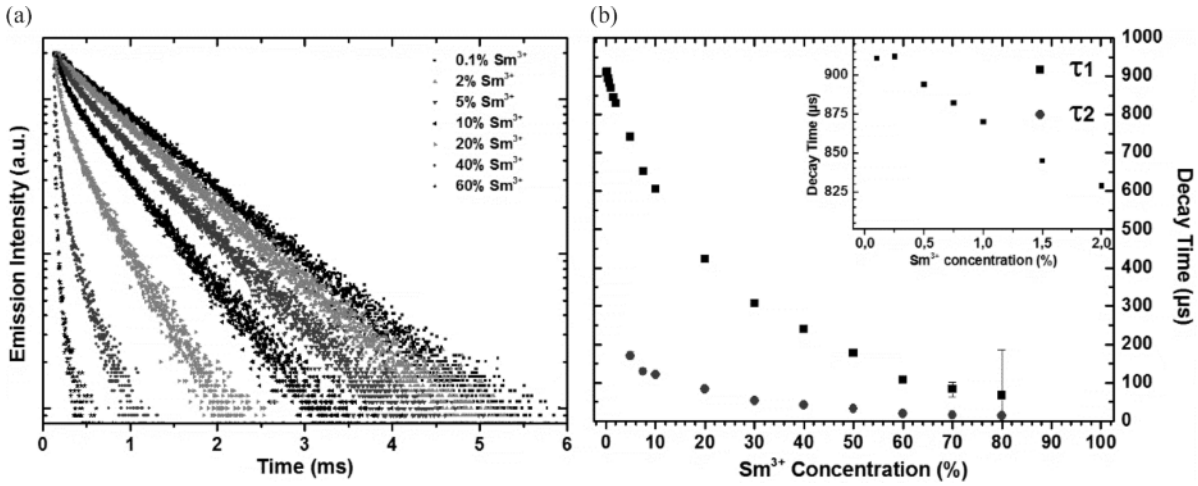

Fig. 5. (a) Decay curves and (b) decay constants of $Li_3Ba_2(La_{1-x}Sm_x)_3(MoO_4)_8$ (λ_{em} = 615 nm, λ_{ex} = 404.5 nm).

perature, the thermal quenching (TQ) $T_{1/2}$ value can be determined. A Boltzman fit of the plot (Fig. 4b) was conducted and revealed a TQ-$T_{1/2}$ of 512 K (±6 K). Furthermore, at 400 K the integrated emission intensity is still at 90 % of its maximum value. Given an operating temperature of an LED of about 420 K, $Li_3Ba_2(La_{1-x}Sm_x)_3(MoO_4)_8$ is a promising candidate for warm-white light-emitting SSL sources.

The decay curves and decay times of the $^4G_{5/2} \rightarrow {}^6H_{5/2}$ transition (645 nm) of $Li_3Ba_2(La_{1-x}Sm_x)_3(MoO_4)_8$ are depicted in Fig. 5. The decay changes from following a mono-exponential to a bi-exponential behavior at concentrations higher than 2 %. That means that two kinds of Sm^{3+} ions with different decay times are observed. Since there are two crystallographic sites available for Sm^{3+} (*M*1 and *M*2) it can be concluded that one site is preferred, and the less preferred one is populated only at sufficiently high concentrations, *i. e.* at more than 2 %. The *M*1 site is larger (av. *M*–O distance 0.2856 nm) and ten-fold coordinated, while the eight-fold coordinated *M*2 site is smaller (av. *M*–O distance 0.2435 nm). *M*1 has a minimum distance of 0.445 nm to the next potential Sm^{3+} site, while for *M*2 this distance is only 0.390 nm [16]. Therefore, we assume that *M*1 exhibits less potential for concentration quenching and is the preferred site for Sm^{3+}. This assumption explains both the bi-exponential decay curve and the decrease of the slope of emission intensity *vs.* concentration observed for samples doped with Sm^{3+} concentrations higher than 2 %. Furthermore, the *M*1 and *M*2 sites occur in a ratio of 1 : 2 per unit cell. Accordingly, with increasing Sm^{3+} concentration the contribution of the fast component (originating from Sm^{3+} ions on the *M*2 site) to the decay curve increases with increasing activator concentration. At 100 % Sm^{3+} the contribution of the fast component should reach 66 %. However, due to very low emission intensity for highly doped samples, no accurate decay times could be calculated from the measurements. The decay constants with their respective percentile contribution up to 70 % Sm^{3+} are listed in Table 1.

As depicted in Fig. 5, the decay constant starts to decrease at a dopant level higher than 0.25 %. Decay constants are proportional to the internal quantum efficiency (*IQE*), which can be expressed by

$$IQE = W_r/(W_r + W_{nr}) \quad (3)$$

where W_r and W_{nr} are the probabilities for radiative and non-radiative transitions to the ground state, respectively [9]. From a decrease of the decay constant a decrease of W_r or an increase of W_{nr} can be concluded. Since the sum of the probabilities W_r and W_{nr} is equal to unity, both processes occur simultaneously. Therefore, the probability of non-radiative transitions, most likely due to cross-relaxation, begins to increase at concentrations as low as 0.5 %. The calculated decay constants for several Sm^{3+} concentrations can be found in Table 1.

Decay curves were recorded for $Li_3Ba_2La_3(MoO_4)_8:Sm^{3+}$ (5 %) at different temperatures as depicted in Fig. 6. Both fitting parameters

Concentration of Sm^{3+} (%)	CIE1931 Color point x, y	Luminous efficacy ($lm\,W^{-1}$)	Quantum efficiency (%)	Decay constants (μs) with percentile contributions for τ_1; τ_2
1	0.633, 0.367	211	36	870; –
2	0.632, 0.367	212	44	829; –
5	0.631, 0.368	214	36	742 (95 %); 170 (5 %)
10	0.632, 0.368	213	23	605 (91 %); 121 (9 %)
20	0.632, 0.367	213	9	423 (81 %); 82.6 (19 %)
30	0.632, 0.368	213	4	307 (73 %); 52.9 (27 %)
40	0.632, 0.368	213	2	240 (69 %); 41.5 (31 %)
50	0.631, 0.368	213	2	177 (58 %); 32.3 (42 %)
70	–	–	1	82.5 (40 %); 15.4 (60 %)
100	–	–	1	– ; –

Table 1. Color points, luminous efficacies, quantum efficiencies and decay constants with their respective contribution of $Li_3Ba_2La_3(MoO_4)_8:Sm^{3+}$ samples with different Sm^{3+} concentrations.

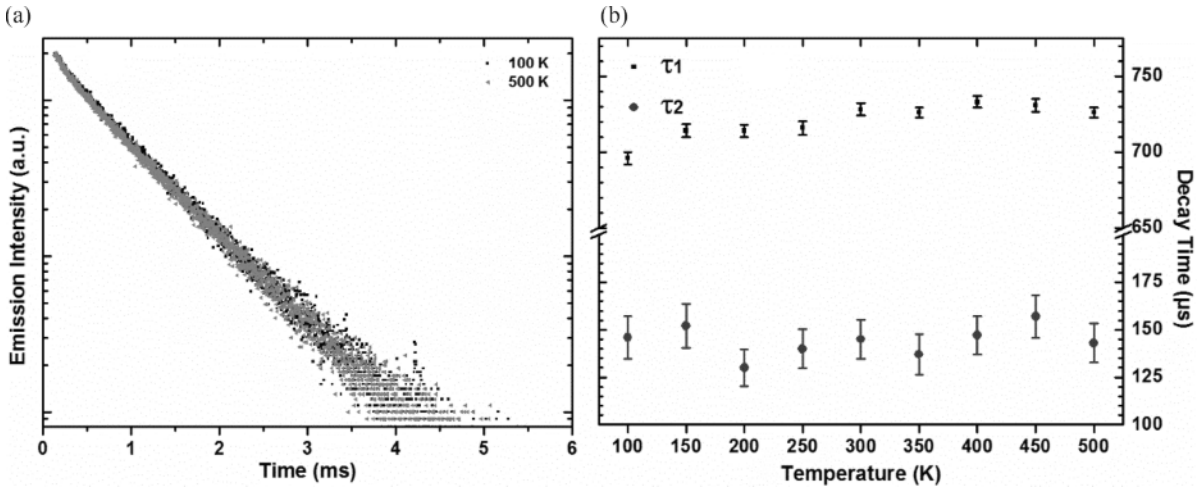

Fig. 6. (a) Decay curves of $Li_3Ba_2La_3(MoO_4)_8:Sm^{3+}$ (5 %) at (black) 100 K and (gray) 500 K upon 404.5 nm excitation; (b) decay constants of the sample at temperatures between 100 and 500 K.

for the decay time remain constant with temperature within the margin of error. As mentioned previously, the decay constant is proportional to the internal quantum efficiency. Thus from the measurement one can conclude that the internal quantum efficiency is not affected by temperature. However, the emission intensity decreases with increasing temperature. The emission intensity is proportional to the external quantum efficiency (*EQE*) if the absorption strength is considered to be independent of temperature. It can be expressed as

$$EQE = IQE \cdot \eta_{esc} \tag{4}$$

where η_{esc} is the escape efficiency of photons from the phosphor particle. In $Li_3Ba_2La_3(MoO_4)_8:Sm^{3+}$ (5 %) the *IQE* is constant with increasing temperature, while its *EQE* decreases. This is only possible if η_{esc} decreases with increasing temperature. The same observation was made for Eu^{3+}-doped $Li_3Ba_2La_3(MoO_4)_8$ [9]. The decrease of the escape efficiency at higher temperatures seems to be inherent to the host material. According to Schwung *et al.* there is always some amount of Mo^{5+} present in $LiEuMo_2O_8$ [30]. If the same holds true for $Li_3Ba_2(La_{1-x}Sm_x)_3(MoO_4)_8$, a low-lying Mo^{5+}/Mo^{6+} intervalence charge transfer (IVCT) state could result in reabsorption of Sm^{3+} emission. Higher temperatures favor the formation of oxygen vacancies in molybdates [31] and consequently the formation of Mo^{5+}. This would explain the decrease of η_{esc} with increasing temperature.

From the emission spectra CIE 1931 color points and luminous efficacies (LE) were calculated. In Fig. 7 fragments of the CIE 1931 color diagram are shown with the respective color points of selected samples. The Black Body Locus (BBL) is also included for

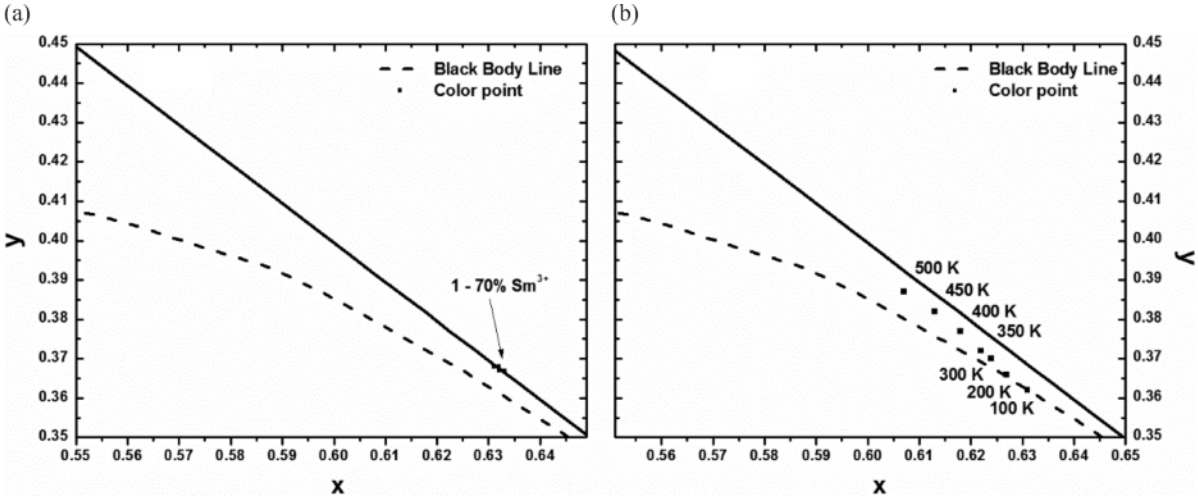

Fig. 7. Color points of (a) $Li_3Ba_2La_3(MoO_4)_8:Sm^{3+}$ with different Sm^{3+} concentrations and of (b) $Li_3Ba_2La_3(MoO_4)_8:Sm^{3+}$ (5 %) at different temperatures (λ_{ex} = 404.5 nm).

reference. When the excitation wavelength was set to 404.5 nm, the color point exhibits no significant shift with increasing Sm^{3+} concentration (Fig. 7a), meaning that the ratio between the emission lines does not change. This behavior could be expected, since all emission lines can be assigned to transitions originating from the $^4G_{5/2}$ level and are equally prone to quenching by cross-relaxation. The deviation observed for the more highly doped samples can be explained by the very low emission intensities. The signal to noise ratio is low, and the margin of error of color points and LE is relatively high. The color point and LE values can be found in Table 1. For the samples with more than 70 % Sm^{3+} no color points could be calculated due to the low emission intensity.

The color points and LE of the 5 % Sm^{3+} sample at different temperatures were calculated from the respective emission spectra. In Fig. 7b the color points are shown in a fragment of the CIE 1931 color diagram. With increasing temperature a blue-shift of the color point can be observed. From a comparison of the emission spectra recorded at 100 and 500 K (Fig. 4a), it can be concluded that it is caused by a blue-shift of the $^4G_{5/2} \rightarrow {}^6H_{9/2}$ emission line. This can be explained by lattice expansion and a subsequent increase of the size of the Sm^{3+} sites. The spin-orbit coupling decreases, resulting in the aforementioned shift. Another possibility is that higher vibronic levels are populated at higher temperatures. That would also result in a blue-shift. The LE increases since a blue-shift from the red spectral region shifts the emission closer to the maximum of the human eye sensitivity curve.

In Table 1 the *EQE* of selected samples are listed. The maximum *EQE* = 44 % was found for the 2 % Sm^{3+}-doped samples. Further increase of the concentration decreases the *EQE*. This is in good agreement with the observation that at concentrations higher than 2 % a second, faster component becomes noticable in the decay curves. The maximum of 44 % is much less than what has been achieved in glassy host structures (*e. g.* 72.5 % in sodium silico-phosphate glasses or ∼ 100 % in sodium fluoroborate glasses [32, 33]). This large difference can be explained by multiphonon relaxation of the NIR-emitting $^4G_{5/2} \rightarrow {}^6F_J$ transitions. As a rule of thumb, if the energy of a transition is lower than approximately 5 times the energy of the highest-energy lattice vibration, a non-radiative transition can occur, generating an appropriate amount of phonons instead of one photon. In glasses, phonon frequencies are generally lower than in crystalline structures. Therefore, often no quenching of Sm^{3+} NIR emission by multi-phonon relaxation is observed in such materials [34, 35], resulting in a significantly higher *QE*.

The morphological features of the synthesized $Li_3Ba_2La_3(MoO_4)_8$, $Li_3Ba_2La_{1.5}Sm_{1.5}(MoO_4)_8$, and $Li_3Ba_2Sm_3(MoO_4)_8$ phosphor powders were inspected by taking the SEM pictures given in Fig. 8. The morphologies show rather large (2 – 5 μm) and regu-

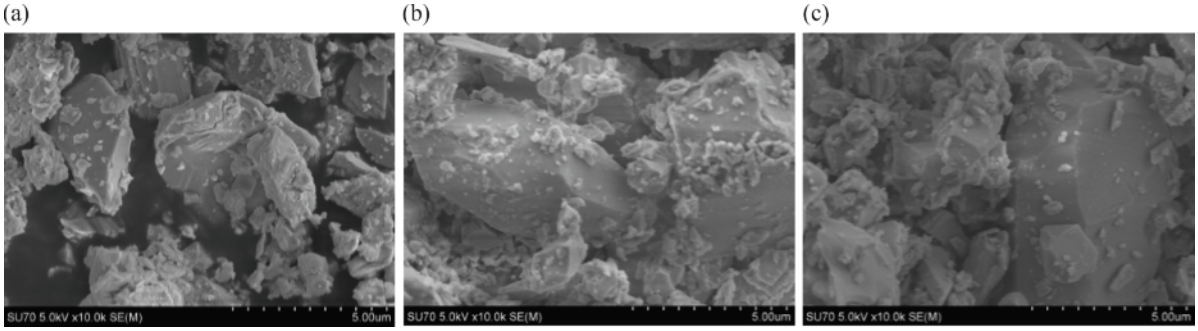

Fig. 8. SEM images of (a) $Li_3Ba_2La_3(MoO_4)_8$, (b) $Li_3Ba_2La_{1.5}Sm_{1.5}(MoO_4)_8$ and (c) $Li_3Ba_2Sm_3(MoO_4)_8$ under magnification of ×5.0 k.

larly shaped particles, which are surrounded by much smaller particles. No significant changes in particle morphology were observed upon increasing the Sm^{3+} content.

Conclusions

In this work Sm^{3+}-doped $Li_3Ba_2La_3(MoO_4)_8$ has been prepared by solid-state synthesis and its optical properties have been characterized. The *intra*-configurational $[Xe]4f^5 \rightarrow [Xe]4f^5$ transitions of Sm^{3+} were assigned to the lines observed in reflection and excitation spectra. By excitation at 404.5 nm several line multiplets in the orange to red spectral region were observed in their emission spectra. Based on the emission spectra and the decay curves it has been concluded that concentration quenching occurs due to cross-relaxation at concentrations as low as 0.5 %. The decay curves revealed that Sm^{3+} occupies two different sites in the material if the concentration is higher than 2 %. One of the sites exhibits a much lower decay constant, indicating a strong quenching process on this site. This behavior was discussed in relation to Sm^{3+}–Sm^{3+} distances within the material, and a multipolar interaction mechanism was assumed.

The decay constants have been shown to remain unchanged with increasing temperature up to 500 K, while the emission intensity decreases strongly at temperatures higher than 450 K. Therefore, the internal quantum efficiency is not influenced by temperature, and the photon escape probability was found to be responsible for the drop in emission intensity at higher temperatures. A maximum *EQE* of 44 % was found in the 2 % sample. This value is much lower than in glassy hosts since in most cases the NIR emission of Sm^{3+} is completely quenched at room temperature in crystalline host materials. The color point does not shift significantly with increasing concentration, however, an increase in temperature results in a blue-shift of the emission. This observation has been explained by a stronger thermal quenching of the lower-energy Stark levels.

Acknowledgement

This work was kindly supported by Merck KGaA, Darmstadt, Germany.

[1] A. A. Setlur, *Electrochem. Soc. Interface* **2009**, *18*, 32 – 36.
[2] E. F. Schubert, J. K. Kim, *Science* **2005**, *308*, 1274 – 1278.
[3] Y. Narukawa, M. Ichikawa, D. Sanga, M. Sano, T. Mukai, *J. Phys. D: Appl. Phys.* **2010**, *43*, 354002.
[4] R. Mueller-Mach, G. O. Mueller, M. R. Krames, T. Trottier, *IEEE J. Sel. Top. Quantum Electron.* **2002**, *8*, 339 – 345.
[5] S. C. Allen, A. J. Steckl, *Appl. Phys. Lett.* **2008**, *92*, 143309 – 143311.
[6] A. Žukauskas, R. Vaicekauskas, F. Ivanauskas, H. Vaitkevičius, M. S. Shur, *Appl. Phys. Lett.* **2008**, *93*, 51115.
[7] M. Born, T. Jüstel, *Chem. Unserer Zeit* **2006**, *40*, 294 – 305.
[8] R. Mueller-Mach, G. O. Mueller, M. R. Krames, H. A. Höppe, F. Stadler, W. Schnick, T. Jüstel, P. Schmidt, *Phys. Status Solidi A* **2005**, *202*, 1727 – 1732.

[9] A. Katelnikovas, J. Plewa, S. Sakirzanovas, D. Dutczak, D. Enseling, F. Baur, H. Winkler, A. Kareiva, T. Jüstel, *J. Mater. Chem.* **2012**, *22*, 22126 – 22134.
[10] M. Brik, A. Srivastava, *J. Lumin.* **2013**, *133*, 69 – 72.
[11] W. Shu, L. Jiang, S. Xiao, X. Yang, J. Ding, *Mater. Sci. Eng. B* **2012**, *177*, 274 – 277.
[12] R. Cao, M. Peng, E. Song, J. Qiu, *ECS. J. Solid State Sci. Technol.* **2012**, *1*, R123 – 126.
[13] Y. Arai, S. Adachi, *J. Lumin.* **2011**, *131*, 2652 – 2660.
[14] S. Sakirzanovas, A. Katelnikovas, H. Bettentrup, A. Kareiva, T. Jüstel, *J. Lumin.* **2011**, *131*, 1525 – 1529.
[15] M. Yamaga, H. Uno, S.-i. Tsuda, J.-P. R. Wells, T. P. Han, *J. Lumin.* **2012**, *132*, 1608 – 1617.
[16] R. F. Klevtsova, A. D. Vasil'ev, L. A. Glinskaya, A. I. Kruglik, N. M. Kozhevnikova, V. P. Korsun, *J. Struct. Chem.* **1992**, *33*, 443 – 447.
[17] J. B. Gruber, B. Zandi, M. F. Reid, *Phys. Rev. B* **1999**, *60*, 15643 – 15655.
[18] X. Y. Chen, M. P. Jensen, G. K. Liu, *J. Phys. Chem. B* **2005**, *109*, 13991 – 13999.
[19] B. Jamalaiah, J. Suresh Kumar, A. Mohan Babu, T. Suhasini, L. Rama Moorthy, *J. Lumin.* **2009**, *129*, 363 – 369.
[20] A. A. Dakhel, *J. Alloy. Comp.* **2004**, *365*, 233 – 239.
[21] J. Yang, B. Zhai, X. Zhao, Z. Wang, H. Lin, *J. Phys. Chem. Solids* **2013**, *74*, 772 – 778.
[22] A. Kumar, D. K. Rai, S. B. Rai, *Spectrochim. Acta A* **2003**, *59*, 917 – 925.
[23] Y.-h. Wang, D.-Y. Wang, *J. Electrochem. Soc.* **2006**, *153*, H166–H169.
[24] T.-W. Kuo, C.-H. Huang, T.-M. Chen, *Optic. Express* **2010**, *18*, A231–A236.
[25] G. Blasse, *Philips Res. Rep.* **1969**, *24*, 131 – 144.
[26] F. Kellendonk, G. Blasse, *Phys. Status Solidi (B)* **1981**, *108*, 541 – 548.
[27] K. K. Mahato, D. K. Rai, S. B. Rai, *Solid State Commun.* **1998**, *108*, 671 – 678.
[28] T. Luxbacher, H. P. Fritzer, C. D. Flint, *J. Phys. Condens. Matter* **1995**, *7*, 9683 – 9692.
[29] S. Surendra Babu, C. K. Jayasankar, P. Babu, *Phys. Chem. Glasses-B* **2006**, *47*, 548 – 552.
[30] S. Schwung, D. Rytz, A. Gross, U.-Ch. Rodewald, R.-D. Hoffmann, B. Gerke, B. Heying, C. Schwickert, R. Pöttgen, T. Jüstel, *Opt. Mater.* **2014**, *36*, 589 – 590.
[31] P. Lacorre, F. Goutenoire, O. Bohnke, R. Retoux, Y. Laligant, *Nature* **2000**, *404*, 856 – 858.
[32] P. Raghava Rao, G. Murali Krishna, M. Brik, Y. Gandhi, N. Veeraiah, *J. Lumin.* **2011**, *131*, 212 – 217.
[33] D. Umamaheswari, B. Jamalaiah, T. Sasikala, I.-G. Kim, L. R. Moorthy, *J. Non-Cryst. Solids* **2012**, *358*, 782 – 787.
[34] T. Suhasini, J. Suresh Kumar, T. Sasikala, K. Jang, H. S. Lee, M. Jayasimhadri, J. H. Jeong, S. S. Yi, L. Rama Moorthy, *Opt. Mater.* **2009**, *31*, 1167 – 1172.
[35] M. Jayasimhadri, E.-J. Cho, K.-W. Jang, H. S. Lee, S. I. Kim, *J. Phys. D: Appl. Phys.* **2008**, *41*, 175101.